Supporting Information

Kiser et al. 10.1073/pnas.1212025109

SI Materials and Methods

Lipid Analysis by TLC. The lipid content of the microsomes, microsomal extracts, and purified retinal pigment epithelium (RPE) 65 was analyzed by TLC. Samples of washed RPE microsomes, 20 mM hexaethylene glycol octyl ether (C_8E_6) microsomal extract, and purified RPE65, each containing 10 µg of total protein were pipetted onto a HPTLC silica gel 60 plate (EMD Chemicals) and dried by application of warm air. Purified phosphatidylcholine, phosphatidylethanolamine, and phosphatidylserine standards were run simultaneously (Avanti Polar Lipids). Plates were developed in a solution consisting of a 65:8:35 vol ratio of 100% chloroform, glacial acetic acid, and 100% methanol. Separated lipids were visualized after incubation of the plate in iodine vapor.

Preparation of RPE Microsomal Extracts for Crystallization Trials. Forty milligrams (wet weight) of RPE microsomes were solubilized with 10 mM Tris·HCl, pH 7, containing 20 or 30 mM C_8E_6 on ice for 15 min. The volume of the solution used for protein extraction was varied between 0.5 mL and 2 mL. Samples were then centrifuged at 150,000 × *g* for 45 min to precipitate insoluble material. Supernatants were concentrated to a final volume of ~40 µL in a 50-kDa MWCO Amicon Ultra–0.5-mL centrifugal device (Millipore) producing a protein concentration of ~10–15 mg/mL and directly used for crystallization trials.

Purification of RPE65 for Crystallization Trials. RPE65 was purified from washed RPE microsomes obtained from 100–300 bovine eyes as previously described with the exception that C_8E_6 was used in place of C_8E_4 for some experiments. RPE65 was also purified using Fos-Choline-10 (Anatrace). Protein was extracted from the RPE of 100 bovine eyes in 10 mM Bis-Tris·HCl, pH 7, containing 1 mM DTT and 22 mM Fos-Choline-10. After 30 min incubation on ice, the sample was centrifuged at 150,000 × *g* for 45 min. RPE65 was purified from the supernatant on a Macro-Prep DEAE column (Bio-Rad) in the presence of 22 mM Fos-Choline-10. RPE65-containing fractions were concentrated to ~100 µL, producing a protein concentration of 10 mg/mL.

RPE65 Crystallization. All crystallization trials were carried out with the hanging-drop vapor-diffusion method. One microliter of concentrated protein sample was added to 1 µL of crystallization solution at room temperature and the drop was allowed to equilibrate against 0.5 mL of crystallization solution at 8 °C.

Crystal form A. Plate-like crystals grown from enzymatically active RPE microsomal extracts were observed after 3–5 d of incubation under several conditions in which PEG 200 was used as the precipitant. However, these crystals were thin and fragile and diffracted poorly. Exhaustive attempts to optimize these crystals by altering components of the crystallization solution were unsuccessful. However, reduction of the volume of extraction buffer used to solubilize microsomes from 1 mL to 0.5 mL resulted in formation of larger and thicker crystals. The best diffracting crystals were grown in a crystallization solution consisting of Tris·HCl, pH 7, containing 30% vol/vol PEG 200 and 3% (wt/vol) PEG 3350. These improved crystals were block or rod shaped and grew to approximate dimensions of 50 × 50 × 200 µm.

Crystal form B. One crystal grown as previously described (0.3 M sodium acetate, pH 8.0, containing 11% wt/vol PEG 3350) using RPE65 purified in C_8E_4 was soaked in a protein-free, synthetic mother liquor containing 1 mM $IrCl_6$ for 48 h and then cryoprotected in synthetic mother liquor supplemented with 15% vol/vol glycerol (condition A). The approximate dimensions of this crystal were ~75 × 75 × 300 µm.

Block-shaped crystals of RPE65 purified in C_8E_6 were grown in a crystallization solution consisting of 100 mM Mes-NaOH, pH 6, and 1 M $(NH_4)_2HPO_4$ (condition B). These crystals appeared within 1 d and grew to full size (~75 × 75 × 150 µm) within 1 wk. They were cryoprotected in protein-free, synthetic mother liquor supplemented with 20% glycerol.

Crystal form C. Oval-shaped crystals of RPE65 purified in Fos-Choline-10 were grown by mixing purified protein solution with 0.1 M sodium cacodylate, pH 6.5, containing 35% (vol/vol) 2-ethoxyethanol. Crystals were observed after 1–2 d and had dimensions of ~50 × 50 × 150 µm.

Phasing and Structural Refinement of the RPE65 Crystals. Crystal form A belongs to space group $P2_12_12_1$. The diffraction was anisotropic with the poorest scattering along the c^* axis. The structure was solved by molecular replacement, using the program Phaser (1) and a single monomer from a previously determined RPE65 structure (PDB ID code 3FSN) as the search model with the membrane-binding regions (residues 195–202 and 261–272) deleted. An RPE65 dimer was located in the asymmetric unit. The model was iteratively refined using phenix.refine (2) and REFMAC (3) and manually refurbished with Coot (4). Non-crystallographic symmetry (NCS) restraints were applied throughout the refinement procedure. The refinement converged to R_{work} and R_{free} values of 22.4% and 26.1% with bond-angle/length rms deviations of 1.09°/0.006 Å, respectively.

Crystal form B, obtained under two different conditions, belongs to space group $P6_522$ with one monomer per asymmetric unit. The structure was solved by the single-wavelength anomalous diffraction (SAD) technique, using data obtained from an Ir-derivatized crystal (condition A) collected at energy just above the Ir L_{III} absorption edge. A single Ir ion was found, using the SHELXC/D/E package (5). The anomalous substructure was completed and refined with Phaser, resulting in an overall figure of merit of 0.215 (6). Density modification in DM (7) allowed automatic model building in ARP/wARP (8). The model was manually completed with Coot and refined against the SAD data in REFMAC (9). Iterative refinement produced a model with $R_{\mathrm{work}}/R_{\mathrm{free}}$ values of 18.5% and 22.9% and bond angle/length rmsds of 1.35°/0.01 Å, respectively. This model was stripped of all heteroatoms with the exception of the catalytic iron atom and directly refined against data obtained from a crystal grown under condition B. Reflections used for cross-validation were maintained between the two datasets. Multiple rounds of REFMAC refinement with TLS *B*-factor refinement (10) followed by manual rebuilding and structure completion produced a model with $R_{\mathrm{work}}/R_{\mathrm{free}}$ values of 21.5% and 24.7% and bond angle/length rmsds of 1.01°/0.005 Å, respectively.

Crystal form C belongs to space group $P6_5$ with two monomers in the asymmetric unit and is essentially isomorphous to the previously reported RPE65 crystals (11). The prior RPE65 structural model (PDB ID code 3FSN) was directly refined against these data after removal of heteroatoms. Reflections used for cross-validation were transferred from the prior dataset. The structure was refined in REFMAC, using local NCS restraints to $R_{\mathrm{work}}/R_{\mathrm{free}}$ values of 19.3%/21.9% and bond angle/length rmsds of 1.09°/0.006 Å, respectively.

A summary of the X-ray diffraction data and refinement statistics is provided in Table 1.

Examination of Orthorhombic RPE65 Crystals for Space Group Misassignment, Lattice Defects, and Adventitious Proteins. Structure solution and refinement of the orthorhombic RPE65 crystals proceeded smoothly without any abnormalities. Nevertheless, the unusual molecular packing observed for these crystals prompted us to examine them for space group misassignment, lattice defects, and the presence of other proteins.

Data were processed in XDS, using the automatic space group assignment feature. Integration was performed assuming *P*1 symmetry (12). Primitive triclinic, monoclinic, and orthorhombic lattices all gave acceptable indexing quality of fit values, indicating that the metric symmetry of the crystal lattice is orthorhombic. R_{meas} (redundancy-independent R_{merge}) (13) values for space groups in these Bravais lattices were 9.7% for *P*1, 11.1% for *P*2, and 10.9% for *P*222. The minimal increase in R_{meas} together with the low lattice distortion index upon imposition of mmm Laue symmetry on the data led us to conclude that the crystal has orthorhombic symmetry, so the dataset was processed in space group *P*222. Reflections of the types 00l, 0k0, and h00 were then examined to help determine the presence or absence of 2_1 screw axes along the three principle crystallographic directions. Odd reflections appeared to be systematically absent for all three types of reflections, suggesting that the space group was $P2_12_12_1$. However, owing to problems with overlapping reflections, the h00 reflections were not recorded to as high a resolution as the other two reflection classes, thus leaving some ambiguity about the presence of a screw axis along the *a* axis. Because of this slight ambiguity in space group assignment, we processed the data in space group *P*222 and performed molecular replacement trials in all enantiomorphous space groups with 222 point group symmetry, using Phaser (1). One monomer from a previously determined RPE65 structure (PDB ID code 3FSN) with deleted membrane-binding regions (residues 195–202 and 261–271) was used as a search probe. Because Matthew's coefficient analysis suggested either two or three molecules per asymmetric unit, we searched for up to three molecules during the molecular replacement trials. Log-likelihood gain (LLG) values were substantially higher for solutions in space group $P2_12_12_1$ (LLG = 5,397) compared with the other space groups (LLG = 1,450 for $P2_122_1$, the next highest solution) and no packing clashes were produced in $P2_12_12_1$ in contrast to the other space groups. In all trials, only two RPE65 molecules were located in the asymmetric unit. These data are all consistent with the space group being correctly identified as $P2_12_12_1$ with two molecules in the asymmetric unit.

The data were further examined for twinning as this defect is relatively common and can give rise to crystal packing abnormalities (14). There was no evidence of epitaxial twinning in the diffraction pattern as the data reduction program accounted for virtually all reflections on every frame. Although merohedral twinning is not permitted in orthorhombic space groups, pseudomerohedral twinning can occur in monoclinic space groups when the unit cell constants have special values as, for example, a crystal in space group $P2_1$ with $\beta \sim 90°$. For this particular example and in the case of perfect or near-perfect pseudomerohedral twinning (i.e., twin fraction ~0.5), the crystal symmetry could masquerade as $P222_1$. The data were reprocessed in space group $P2_1$ and analyzed for pseudomerohedral twinning, using phenix.xtriage (15). No twinning was detected and the analysis confirmed the 222 point group symmetry of the crystal.

Order–disorder or lattice translocation defects (LTDs) can give rise to crystal packing arrangements with apparently missing layers of molecules, which led us to closely examine the data for signs of this pathology (16). LTDs are manifested in the diffraction pattern as streaky or diffuse profiles for certain reflections as well as in the native Patterson map as strong nonorigin peaks (17). Such pathological reflections were not evident in the raw diffraction data (Fig. S3*A*). The native Patterson map also did not contain unexplained strong peaks (Fig. S3*B*). Absence of these two hallmark features allowed us to rule out LTDs as the cause of the peculiar crystal packing.

Whereas the crystal packing "gap" was too narrow to accommodate additional RPE65 molecules, it is conceivable that a smaller protein could fit into the gap, although there was no evidence of additional protein components in the electron density maps. To ensure that electron density was not suppressed by the use of the mask bulk solvent model, we also used the Babinet bulk solvent model during refinement. The resulting electron density maps were consistent with those calculated with application of the mask bulk solvent model. Because the sample used to grow the orthorhombic crystal was not homogenous in terms of protein components, we also considered the possibility that another protein could mediate contacts between layers of RPE65 molecules, albeit in a highly disordered fashion. To test this hypothesis, crystals were removed from the mother liquor, washed twice in crystallization solution, dissolved in water, and subjected to SDS/PAGE followed by silver staining. The resulting gel showed only a single band at a mass consistent with that of RPE65, leading us to reject this hypothesis as well (Fig. S2*C*).

X-Ray Absorption Spectroscopy Data Collection and Analysis. Fe K-edge X-ray absorption spectroscopy (XAS) data were collected on beamline X3B of the National Synchrotron Light Source (NSLS). XAS data were obtained as fluorescence excitation spectra, using a 31-element solid-state germanium detector array (Canberra) over an energy range of 6,930–7,810 eV ($k = 13.5$ Å^{-1}). Internal energy calibration was provided by simultaneous measurement of spectra from an iron foil. The energy of the first inflection point of the foil K-edge was assigned as 7,112.0 eV. A Mn filter was used to attenuate background scattering.

The raw XAS data were examined and averaged, and the extended X-ray absorption fine-structure (EXAFS) signal $\chi(k)$ was extracted, with the EXAFSPAK package (18). The program pySpline was used to determine optimal parameters for the spline function used in EXAFSPAK (19). Individual XAS scans for the $\mathbf{RPE65_{red}}$ and $\mathbf{RPE65_{ox}}$ datasets were examined for evidence of photoreduction in the form of a red shift of the Fe K-edge energy. No photoreduction was observed for $\mathbf{RPE65_{red}}$, but a significant red shift was noted for $\mathbf{RPE65_{ox}}$, which appeared to be complete within three scans. The two apocarotenoid oxygenase (ACO) samples exhibited similar properties, with $\mathbf{ACO_{ox}}$ being readily photoreduced within two scans, whereas $\mathbf{ACO_{red}}$ did not exhibit any evidence of radiation damage. X-ray absorption near-edge spectra (XANES) data were normalized with the AUTOBK routine implemented in Athena (20) and first and second derivatives of the XANES were calculated by using a 0.75-eV polynomial smooth.

EXAFSPAK was used to analyze the k^3-weighted EXAFS for $\mathbf{RPE65_{red}}$, using theoretical phase and amplitude parameters obtained with FEFF 8.40 (21) for simple models of the RPE65 active site. In all refinements of EXAFS data, the amplitude reduction factor S_0 was fixed at 0.9, whereas the edge shift parameter ΔE_0 was allowed to float as a single value for all shells. E_0, the point where $k = 0$ Å^{-1}, was defined as 7,130 eV. The coordination number (n) of a given shell was a fixed parameter that was varied iteratively whereas bond lengths (r) and Debye–Waller factors (σ^2) were allowed to freely float with some modifications for fits involving coordinated imidazoles, which were treated as rigid bodies in the refinement. The simple goodness-of-fit parameter F was defined as $\Sigma(\chi_{\mathrm{exptl}} - \chi_{\mathrm{calc}})^2$. For unfiltered data, a second goodness-of-fit parameter, F-factor, was defined as $[\Sigma\, k^6(\chi_{\mathrm{exptl}} - \chi_{\mathrm{calc}})^2/\Sigma\, k^6\chi_{\mathrm{exptl}}{}^2]^{1/2}$. Fits to Fourier-filtered data used the goodness-of-fit criterion F', which corrects for the effect that additional variables have on improving fit quality and is used to compare fits with differing numbers of shells (22). $F' = F^2/N_{\mathrm{IDP}} - \rho$, where ρ is the number of floated variables in the fit and N_{IDP} is the number of independent data points defined as $N_{\mathrm{IDP}} = 2\Delta k \Delta R/\pi$. In the latter equation, Δk is the k-range over which the data are fitted and ΔR is the back-transformation range used in fitting Fourier-filtered data. The appropriateness of first-shell fits was also assessed by using bond valence sum (BVS) analysis (23).

1. McCoy AJ, et al. (2007) Phaser crystallographic software. *J Appl Cryst* 40:658–674.
2. Adams PD, et al. (2010) PHENIX: A comprehensive Python-based system for macromolecular structure solution. *Acta Crystallogr D Biol Crystallogr* 66:213–221.
3. Murshudov GN, et al. (2011) REFMAC5 for the refinement of macromolecular crystal structures. *Acta Crystallogr D Biol Crystallogr* 67:355–367.
4. Emsley P, Cowtan K (2004) Coot: Model-building tools for molecular graphics. *Acta Crystallogr D Biol Crystallogr* 60:2126–2132.
5. Sheldrick GM (2010) Experimental phasing with SHELXC/D/E: Combining chain tracing with density modification. *Acta Crystallogr D Biol Crystallogr* 66:479–485.
6. Read RJ, McCoy AJ (2011) Using SAD data in Phaser. *Acta Crystallogr D Biol Crystallogr* 67:338–344.
7. Winn MD, et al. (2011) Overview of the CCP4 suite and current developments. *Acta Crystallogr D Biol Crystallogr* 67:235–242.
8. Langer G, Cohen SX, Lamzin VS, Perrakis A (2008) Automated macromolecular model building for X-ray crystallography using ARP/wARP version 7. *Nat Protoc* 3:1171–1179.
9. Skubák P, Murshudov GN, Pannu NS (2004) Direct incorporation of experimental phase information in model refinement. *Acta Crystallogr D Biol Crystallogr* 60: 2196–2201.
10. Winn MD, Isupov MN, Murshudov GN (2001) Use of TLS parameters to model anisotropic displacements in macromolecular refinement. *Acta Crystallogr D Biol Crystallogr* 57:122–133.
11. Kiser PD, Golczak M, Lodowski DT, Chance MR, Palczewski K (2009) Crystal structure of native RPE65, the retinoid isomerase of the visual cycle. *Proc Natl Acad Sci USA* 106: 17325–17330.
12. Kabsch W (2010) Integration, scaling, space-group assignment and post-refinement. *Acta Crystallogr D Biol Crystallogr* 66:133–144.
13. Diederichs K, Karplus PA (1997) Improved R-factors for diffraction data analysis in macromolecular crystallography. *Nat Struct Biol* 4:269–275.
14. Yeates TO (1997) Detecting and overcoming crystal twinning. *Methods Enzymol* 276: 344–358.
15. Zwart PH, Grosse-Kunstleve RW, Lebedev AA, Murshudov GN, Adams PD (2008) Surprises and pitfalls arising from (pseudo)symmetry. *Acta Crystallogr D Biol Crystallogr* 64:99–107.
16. Tsai Y, Sawaya MR, Yeates TO (2009) Analysis of lattice-translocation disorder in the layered hexagonal structure of carboxysome shell protein CsoS1C. *Acta Crystallogr D Biol Crystallogr* 65:980–988.
17. Hare S, Cherepanov P, Wang J (2009) Application of general formulas for the correction of a lattice-translocation defect in crystals of a lentiviral integrase in complex with LEDGF. *Acta Crystallogr D Biol Crystallogr* 65:966–973.
18. George GN (2000) EXAFSPAK (Stanford Synchrotron Radiation Lightsource, SLAC National Accelerator Laboratory, Stanford, CA).
19. Tenderhold A, Hedman B, Hodgson KO (2007) pySPLINE: A modern cross-platform program for the processing of raw averaged XAS, edge and EXAFS data. *XAFS13 Conf Proc* 882:105–107.
20. Ravel B, Newville M (2005) ATHENA, ARTEMIS, HEPHAESTUS: Data analysis for X-ray absorption spectroscopy using IFEFFIT. *J Synchrotron Radiat* 12:537–541.
21. Ankudinov AL, Ravel B, Rehr JJ, Conradson SD (1998) Real-space multiple-scattering calculation and interpretation of x-ray-absorption near-edge structure. *Phys Rev B* 58: 7565–7576.
22. Riggs-Gelasco PJ, Stemmler TL, Penner-Hahn JE (1995) XAFS of dinuclear metal sites in proteins and model compounds. *Coord Chem Rev* 144:245–286.
23. Liu W, Thorp HH (1993) Bond valence sum analysis of metal-ligand bond lengths in metalloenzymes and model complexes. 2. Refined distances and other enzymes. *Inorg Chem* 32:4102–4105.

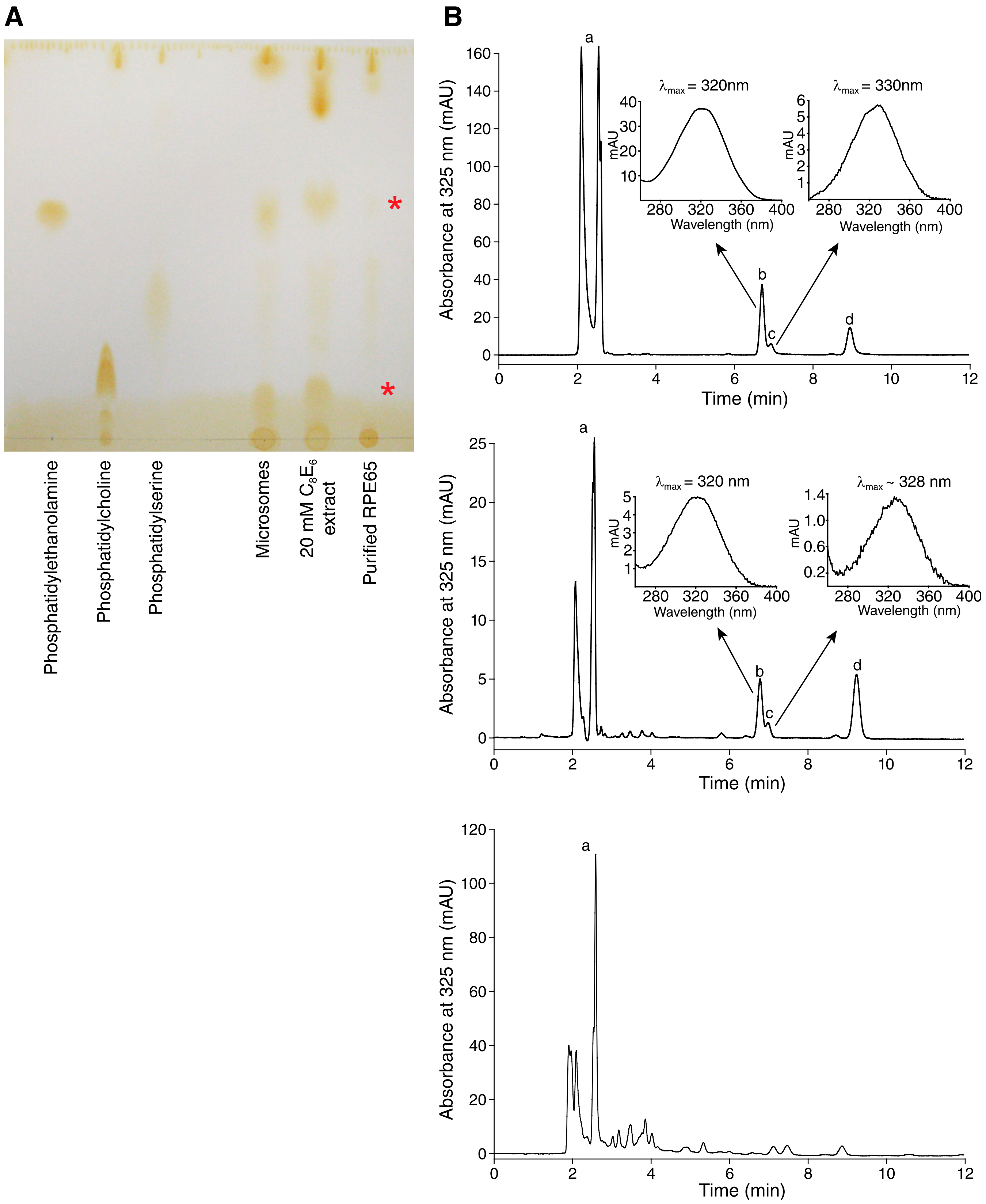

Fig. S1. Lipid composition and enzymatic activity of RPE microsomes, microsomal extracts, and purified RPE65. (*A*) Analysis of lipid composition by TLC. Untreated RPE microsomes and the microsomal detergent extracts display a similar phospholipid composition with phosphatidylcholine (PC) and phosphatidylethanolamine (PE) constituting the major lipids. These lipids are removed during purification of RPE65 on DEAE resin as shown by the absence of lipid staining next to the red asterisks. Phosphatidylserine is retained in the purified RPE65 preparation likely because of either coelution from the anion-exchange column or direct binding to RPE65. (*B*) Chromatograms from the analysis of retinoid isomerase activity in RPE microsomes (*Top*), a 20-mM C_8E_6 extract of RPE

Legend continued on following page

microsomes (*Middle*), or DEAE-purified RPE65 (*Bottom*). Retinoids were identified on the basis of their retention times and absorbance spectra as follows: *a*, all-*trans*-retinyl esters; *b*, 11-*cis*-retinol; *c*, 13-*cis*-retinol; and *d*, all-*trans*-retinol. *Insets* show the clear spectral distinction between 11-*cis*- and 13-*cis*-retinol. Retinoid isomerase activity is observed for RPE microsomes and microsomal detergent extracts but not for purified RPE65.

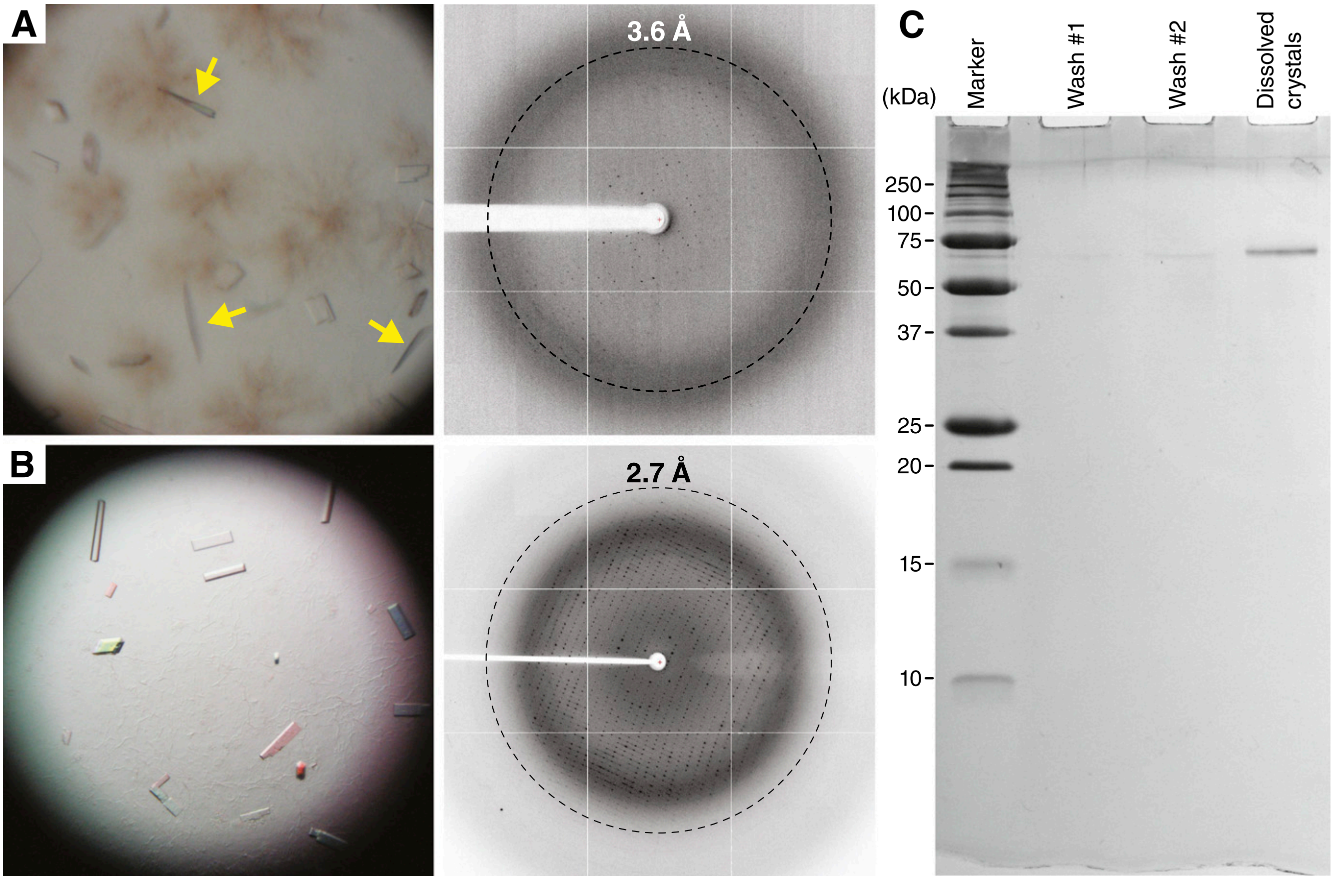

Fig. S2. Dependence of crystal growth and diffraction properties on the sample lipid-to-detergent ratio. (*A*) Initial crystals grown from RPE65 solubilized in 1 mL of buffered solution containing 30 mM C_8E_6 were thin and tended to bend during growth, resulting in poor diffraction. Yellow arrows indicate crystals growing edge-on, showing their thin and bent morphology. (*B*) An increase in the sample lipid/detergent ratio led to growth of thicker crystals with greatly improved diffraction properties. (*C*) SDS/PAGE analysis shows the presence of a single ~65-kDa protein in the crystal. Proteins were visualized by silver staining.

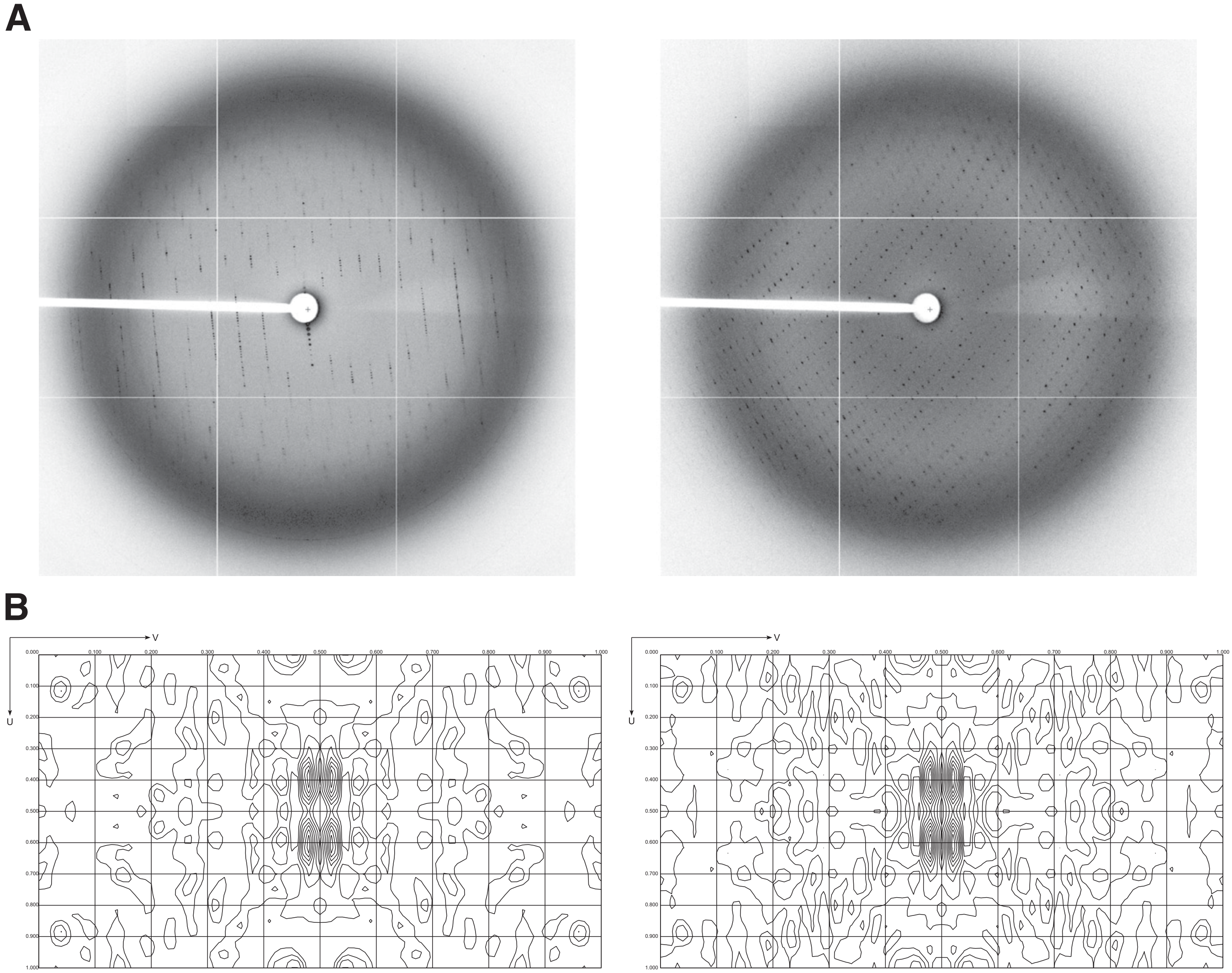

Fig. S3. Analysis of orthorhombic RPE65 crystals for lattice translocation defects (LTDs). (*A*) Raw diffraction images recorded from an orthorhombic RPE65 crystal showing well-defined spots and lack of smearing typically associated with LTDs. The two images are separated by ~45°. (*B*) Experimental (*Left*) and calculated (*Right*) native Patterson maps for the w = 1/2 Harker section, which contained the only significant, nonorigin peak in the map. The peak, which is due to the twofold NCS axis being nearly parallel to the crystallographic c axis, is fully accounted for by the model as shown in the calculated map section. The absence of strong unexplained peaks is consistent with the lack of LTDs.

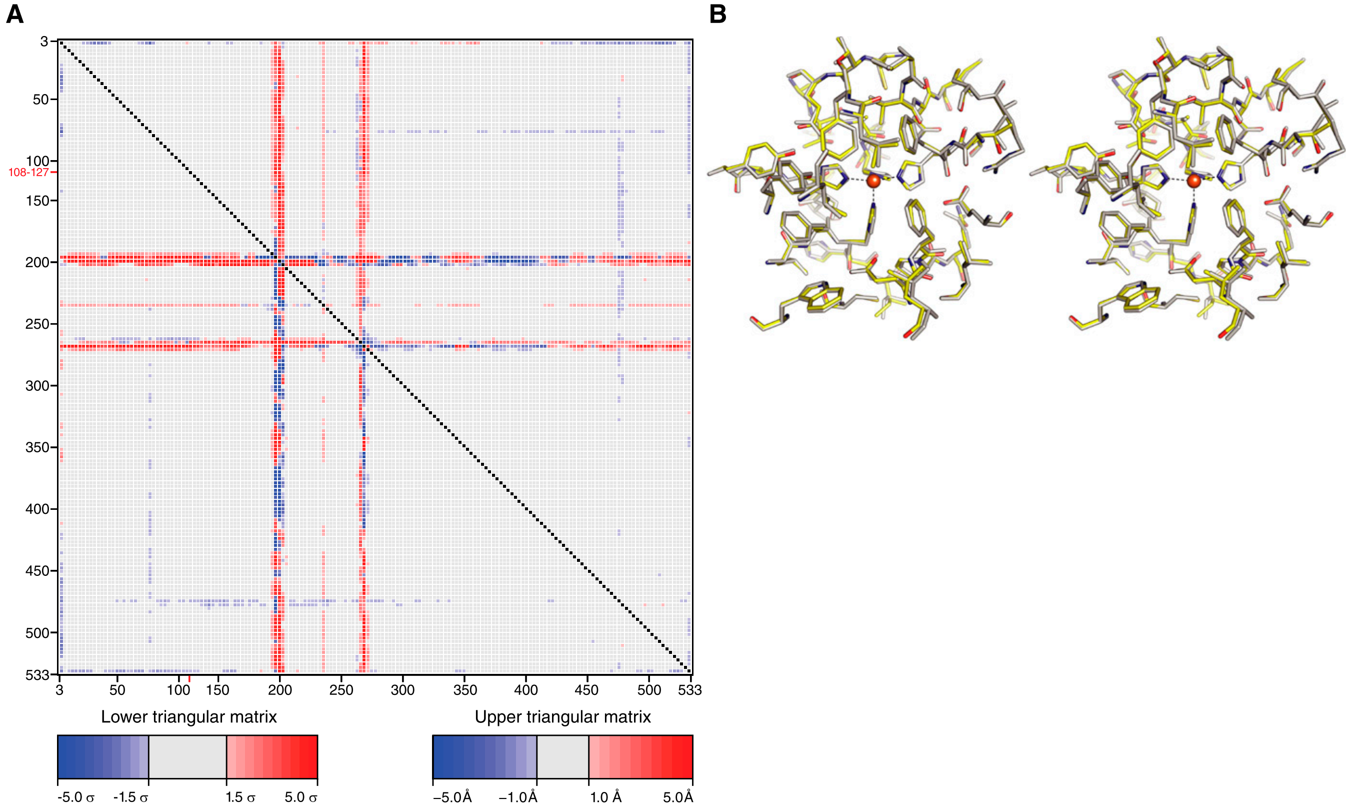

Fig. S4. Structural comparison of lipid-embedded and delipidated RPE65 structures. (*A*) Difference distance matrix analysis of the lipid-embedded structure vs. the delipidated structure. The lower triangular matrix is an error-scaled matrix generated using Cruickshank's diffraction precision index (DPI) (1), whereas the upper triangular matrix is an absolute difference distance matrix (2). Red and blue elements indicate relative structural expansion and contraction, respectively, whereas gray indicates structural invariance. (*B*) Structural superposition of active-site residues in the lipid-embedded (yellow) and delipidated (gray) structures. Residues within 11 Å of the iron cofactor are displayed as sticks and the iron cofactor is shown as an orange sphere. No significant differences are observed between the two structures. The superposition is shown as a wall-eye stereo pair.

1. Cruickshank DW (1999) Remarks about protein structure precision. *Acta Crystallogr D Biol Crystallogr* 55:583–601.
2. Schneider TR (2000) Objective comparison of protein structures: Error-scaled difference distance matrices. *Acta Crystallogr D Biol Crystallogr* 56:714–721.

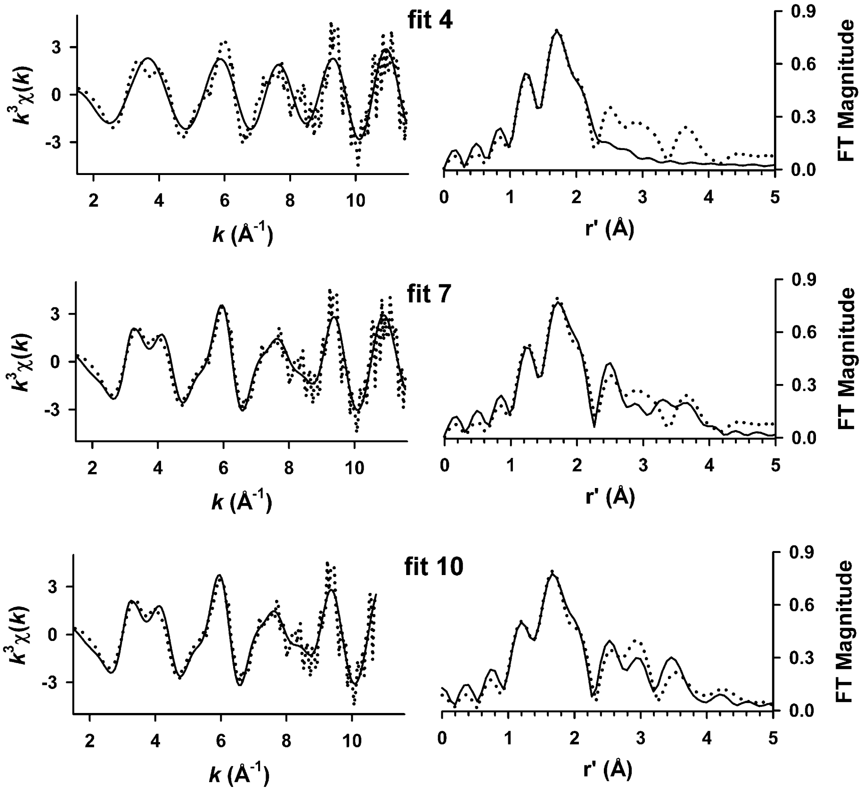

Fig. S5. Several representative fits to the $k^3\chi(k)$ EXAFS and Fourier transforms for detergent-solubilized RPE65. Experimental data are shown with dotted lines, and fit curves are shown with solid lines. The fits shown correspond to those given in Table S2.

Table S1. Fourier-filtered, first-shell EXAFS analyses of isolated RPE65

	Fe-N/O			Fe-O/N			Fe•••C/O					
Fit	*n*	*r*	σ^2	*n*	*r*	σ^2	*n*	*r*	σ^2	*F*′	ΔE_0	BVS
1	4	2.14	5.8							260.7	3.41	1.47
2	5	2.13	8.6							527.4	2.50	1.88
3	6	2.12	12.0							892.1	1.17	2.34
4	4	2.12	2.9	1	1.90	1.0				23.0	−1.79	2.15
5	3	2.13	0.6	1	1.92	1.3				12.9	−1.05	1.68
6	3	2.13	0.7	2	1.93	6.5				18.3	−3.72	2.19
7	5	2.11	5.1	1	1.87	0.8				62.8	−2.53	2.63
8	4	2.12	2.5	2	1.91	5.7				39.3	−4.45	2.70
9	***4***	***2.11***	***3.6***	***1***	***1.89***	***1.9***	***1C***	***2.51***	***0.7***	***2.7***	***−2.69***	***2.19***
10	5	2.10	6.1	1	1.86	1.7	1C	2.50	−0.4	7.8	−3.57	2.69
11	4	2.13	3.2	1	1.91	2.7	2C	2.49	7.9	4.1	−0.31	2.08
12	4	2.14	6.7				1C	2.50	−0.1	77.4	4.06	1.45
13	5	2.13	9.9				1C	2.49	−2.4	156.8	2.31	1.87
14	6	2.12	13.3				1C	2.49	−3.2	287.8	0.28	2.35
15	*4*	*2.12*	*3.5*	*1*	*1.90*	*2.5*	*1O*	*2.46*	*4.7*	*3.8*	*−1.07*	*2.11*
16	5	2.11	6.0	1	1.87	2.2	1O	2.46	2.6	7.4	−2.13	2.60

k_{range} = 1.5–11.6 Å^{-1}, back-transformation range = 0.6–2.4 Å, resolution = 0.156 Å, *r* is in units of Å, σ^2 is in units of 10^{-3} Å^2, and ΔE_0 is in units of eV. Fits of the N/O shell used parameters for an N scatterer, whereas those of the O/N shell used parameters for an O scatterer. EXAFS cannot distinguish between scatterers differing by $Z = 1$. The BVS was calculated using r_0 = 1.769 Å for Fe(II)–N and r_0 = 1.700 Å for Fe(II)–O. The goodness-of-fit parameter *F*′ is defined as $[\Sigma(\chi_{\text{exptl}} - \chi_{\text{calc}})^2]^2/N_{\text{IDP}} - N_{\text{VAR}}$, where N_{IDP} is the number of independent data points, whereas N_{VAR} is the number of floated variables in each optimization step. *F*′ is a measure of whether an added shell significantly improves the fit. The fit shown in bold italics represents the best fit to the experimental data, whereas the fit shown in italics is an alternate good fit.

Table S2. Multiple-scattering EXAFS analysis of isolated RPE65

	Fe-N/O			Fe•••C/O			Fe•••His MS					
Fit	*n*	*r*	σ^2	*n*	*r*	σ^2	*n*	*r*	σ^2	*F*	ΔE_0	BVS
1	4N	2.15	5.1							0.671	4.24	1.44
2	5N	2.14	7.9							0.721	3.23	1.84
3	4N	2.12	2.1							0.551	−1.34	2.11
	1O	1.91	−0.3									
4	*4N*	*2.13*	*3.3*	*1C*	*2.48*	*−0.5*				*0.523*	*−0.96*	*2.08*
	1O	*1.91*	*1.9*									
5	4N	2.14	2.6	1O	2.43	3.0				0.523	0.48	2.16
	1O	1.92	1.5									
6	4N	2.16	3.3	1C	2.46	−0.8	8	3.12/	9.7/	0.469	3.95	1.92
	1O	1.94	4.1				16	3.27/				
7	***4N***	***2.15***	***3.2***	***1C***	***2.46***	***−0.4***	***4 His***	***3.12/ 3.26/***	***10.0/***	***0.428***	***2.18***	***1.98***
	1O	***1.93***	***3.2***					***4.38# 4.35# 4.41#***	***12.1#***			
8	4N	2.15	3.0	1C	2.46	0.3	3 His	3.12/ 3.26/	7.5/	0.420	2.01	1.99
	1O	1.93	2.7					4.37# 4.34# 4.41#	8.2#			
9	4N	2.15	2.3	1O	2.40	3.1	4 His	3.12/ 3.26/	9.6/	0.430	2.14	2.12
	1O	1.93	1.6					4.38# 4.35# 4.41#	12.0#			
10	*4N*	*2.15*	*2.7*	*1C*	*2.46*	1.0^*	*4 His*	*3.11/ 3.26/*	*9.4/*	*0.396*	*2.06*	*1.99*
	1O	*1.93*	*2.1*					*4.38# 4.35# 4.41#*	*11.0#*			

k_{range} = 1.5–11.6 Å^{-1}, resolution = 0.156 Å, *r* is in units of Å, and σ^2 is in units of 10^{-3} Å^2. $F = [\Sigma k^6(\chi_{exptl} - \chi_{calc})^2/\Sigma^6 \chi_{exptl}{}^2]^{1/2}$. Scattering paths for coordinated His are given in two sets denoted as "/" and "#." The two paths at 3.12 and 3.26 Å correspond to single and multiple scattering involving His Cα, whereas the three paths at 4.3–4.4 Å correspond to single and multiple scattering involving His Cβ/Nβ. Within these sets, σ^2 was floated at a common value, whereas *r* values were constrained to a constant difference from each other. The BVS was calculated using r_0 = 1.769 Å for Fe(II)–N and r_0 = 1.700 Å for Fe(II)–O. The k_{range} for fit 10 was 1.5–10.75 Å.The fit in bold italics represents the best fit to the experimental data shown in Fig. 6 and Fig. S5, whereas those in italics are alternate good fits shown in Fig. S5.

*Parameters were fixed during refinement.

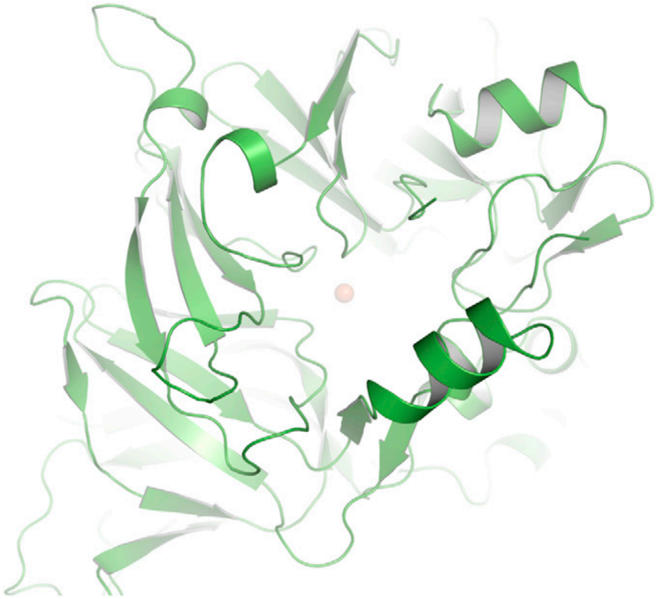

Movie S1. Conformational differences between lipid-embedded and delipidated RPE65. The movie begins with the delipidated structure and morphs into the lipid-embedded structure. The morph was generated with Rigimol (Schrodinger) and the movie was created with PyMOL (Schrodinger) and Adobe Photoshop.

Movie S1